



La_{1-x}Sr_xCo_{1-y}Fe_yO_{3-δ} perovskites: Preparation, characterization and solar photocatalytic activity

E. García-López^{a,**}, G. Marci^a, F. Puleo^b, V. La Parola^b, L.F. Liotta^{b,*}

^a "Schiavello-Grillone" Photocatalysis Group, Dipartimento di Energia, Ingegneria dell'informazione e modelli Matematici (DEIM), Università di Palermo, Viale delle Scienze, 90128 Palermo, Italy

^b Istituto per Lo Studio dei Materiali Nanostrutturati (ISMN)-CNR, via Ugo La Malfa, 153, 90146 Palermo, Italy



ARTICLE INFO

Article history:

Received 9 July 2014

Received in revised form 3 September 2014

Accepted 7 September 2014

Available online 16 September 2014

Keywords:

Lanthanocobaltites

Photocatalysis

Solar irradiation

2-Propanol

ABSTRACT

LaCoO₃ perovskites substituted by Sr at the A site and/or by Fe at the B site have been prepared by the citrate method. Characterizations by several techniques, such as specific surface area (BET method), XRD, TPR, SEM, UV–vis in DRS mode, XPS and TGA analyses, have been performed.

The so prepared La_{1-x}Sr_xCo_{1-y}Fe_yO_{3-δ} perovskites are semiconductor materials showing band gap energy values from 1.9 to 3.2 eV. They displayed solar photocatalytic activity for the 2-propanol degradation in gas–solid regime. The photocatalytic results suggest that the perovskites containing Fe are less active and the activity decreases by increasing the Fe content, however the presence of iron avoids the catalyst deactivation. The best photocatalytic activity in the 2-propanol degradation was found for the sample La_{0.6}Sr_{0.4}CoO_{3-δ}.

© 2014 Elsevier B.V. All rights reserved.

1. Introduction

The utilization of solar light as an efficient radiation source for photocatalytic purposes has been largely pursued and considerable efforts have been invested to develop photocatalysts which utilize the visible light that accounts for the 43% of the solar spectrum. The strategy traditionally explored has been the modification of TiO₂ based materials for instance by photosensitizing the surface with suitable dyes or by doping with transition metal or non-metal elements; however, the success of these methodologies has been moderate [1,2]. Small band energy semiconductors such as CdS, CdSe, Fe₂O₃ or WO₃ have been also proposed but they have resulted deficient in either activity or stability [1,2]. The development of alternative photocatalytic materials active under visible light irradiation ($\lambda > 400$ nm) is still an important subject of research [2–4]. In this context a number of perovskites such as SrTiO₃ [5], BiVO₄ [6,7], LaCoO₃ [8] and Bi₂WO₆ [9] have been demonstrated as promising photocatalysts for oxidation reactions, mainly in liquid–solid regime, showing a strong visible light absorption and high quantum efficiency. These oxides have also showed a better

photocatalytic activity than TiO₂ irradiated by sunlight or visible light irradiation for direct water splitting to H₂ and O₂ [10].

Perovskite-type oxides ABO₃, where A is a rare earth cation and B a transition metal one, present electrical, mechanical, optical, magnetic and catalytic properties. These materials have been widely used as electrode materials for solid oxide fuel cells [11], chemical sensors [12], oxygen-permeating membranes [13], thermo-electric devices [14] and catalysts [15]. Their unique features such as various types of oxygen vacancy order [16], intrinsic oxygen reduction activity [17], high conductivity [18], magnetic properties [19], and excellent performance as cathode or anode [20] have focused the research attention.

Lanthanum cobaltite (LaCoO₃) is a cheap, environmentally friendly and highly catalytically active material in oxidation processes. These features make it a very promising material for many applications. The perovskite oxides based on lanthanum strontium cobalt ferrite (La_{1-x}Sr_xCo_{1-y}Fe_yO_{3-δ}) are the most studied mixed ionic and electronic conducting (MIEC) materials for cathode applications in solid oxide fuel cells [21].

The perovskite-type LaCoO₃ have been also proposed as photocatalysts for wastewater treatments. Fu et al. [22] have prepared LaCoO₃ perovskite-type oxides as hollow nanospheres and investigated their photocatalytic activity for the degradation of methylene blue, methyl orange and neutral red. Jiang and Wei [23] have prepared the LaCoO₃ perovskite by sol–gel process and they have studied the photocatalytic activity for dyes bleaching. Also one-dimensional LaCoO₃ nanostructure was prepared and tested for

* Corresponding author.

** Corresponding author. Tel.: +39 09123863784.

E-mail addresses: elisaisabel.garcialopez@unipa.it (E. García-López), liotta@pa.ismn.cnr.it (L.F. Liotta).

the rhodamine B decomposition under UV light [24]. Ba-doped LaCoO_3 with different Ba contents was also prepared and used for the degradation of malachite green under UV and visible light irradiation [25]. The Ba doping gave rise to the coexistence of Co^{3+} and Co^{4+} in the perovskite along with an increase of oxygen vacancies. Yamada et al. [26] have tested some cobalt-containing perovskites (LaCoO_3 , NdCoO_3 , YCoO_3 , $\text{La}_{0.7}\text{Sr}_{0.3}\text{CoO}_3$) for photocatalytic water oxidation with $\text{Na}_2\text{S}_2\text{O}_8$ and $[\text{Ru}(\text{bpy})_3]^{2+}$ as an electron acceptor and a photosensitizer, respectively. The photocatalysts with the perovskite structure exhibited higher catalytic activity as compared with spinel or wolframite structures. LaCoO_3 , which stabilizes Co^{3+} species in the perovskite structure, exhibited the highest activity compared with CoWO_4 , Co_3O_4 and $\text{La}_{0.7}\text{Sr}_{0.3}\text{CoO}_3$ which contain Co^{2+} or Co^{4+} species in the matrices. There is an agreement affirming that the structures and properties of the LaCoO_3 based materials, such as crystallite diameter, morphology, and crystalline phases associated with their catalytic/photocatalytic performance, highly depend on the synthesis methodology, precursor and/or dopants [27].

In the present work perovskite oxides based on LaCoO_3 has been prepared by substituting the La cation by Sr and the Co cation by Fe. The resulting lanthanum strontium cobalt ferrite ($\text{La}_{1-x}\text{Sr}_x\text{Co}_{1-y}\text{Fe}_y\text{O}_{3-\delta}$) materials have been characterized and tested as photocatalysts in gas–solid regime by using natural solar light as irradiation source.

2. Experimental

2.1. Samples preparation

Nanostructured $\text{La}_{1-x}\text{Sr}_x\text{Co}_{1-y}\text{Fe}_y\text{O}_{3-\delta}$ perovskites with variable Sr and Fe content ($x = 0.0\text{--}0.5$ and $y = 0.0\text{--}0.8$) were synthesized by the sol–gel citrate method starting from the metal nitrates as precursors [28]. The metal nitrates, weighed according to the nominal compositions, were dissolved in a minimum quantity of deionized water. Citric acid (molar ratio of citric acid/metals = 1.5) was added to this solution and finally ammonia (28–30%) was dripped until pH 9–10. The resulting solution was then concentrated, under constant stirring, by heating in oil bath at 90°C and dried heating at 120°C overnight. The recovered powder was calcined at 350°C for 1 h to promote citrate decomposition and hence at 800°C for 4 h (heating rate $5^\circ\text{C}/\text{min}$). The obtained perovskites were labelled as LSCF followed by four numbers where the first two indicate the molar ratio between lanthanum (L) and strontium (S) and the second two the molar ratio between cobalt (C) and iron (F). For instance the $\text{La}_{0.6}\text{Sr}_{0.4}\text{Co}_{0.2}\text{Fe}_{0.8}\text{O}_{3-\delta}$ sample was labelled as LSCF6428. The bare LaCoO_3 perovskite was labelled as LC. Table 1 lists the chemical composition and labelled name of the prepared samples.

2.2. Characterization of the solids

The physico-chemical characterization of the samples was performed by the techniques described in the following: specific surface area (SSA) measurements were performed using a

Sorptomatic 1900 Carlo Erba Instrument, by physical adsorption of N_2 at the temperature of liquid nitrogen (-196°C), using the BET method in the standard pressure range of $0.05\text{--}0.30\text{ p/p}_0$ [29].

XRD measurements were carried out with a Bruker D5000 vertical goniometer equipped with Cu anode ($K\alpha$ radiation = 1.5418 \AA) and a graphite monochromator. A proportional counter and a 0.05° step size in 2θ were used. The integration time was 5 s per step and the scan range was from 20° to 80° in 2θ . The assignment of the various crystalline phases in 2θ was based on the Inorganic Crystal Structure database (ICSD, FIZ Karlsruhe) [30]. The crystallite dimensions were estimated through the line-broadening (LB) of the available reflection peaks, using the Scherrer equation [31].

Temperature programmed reduction (TPR) experiments were carried out with a Micromeritics Autochem 2950 apparatus equipped with a thermal conductivity detector (TCD). A gas mixture H_2 5 vol% in Ar (30 ml min^{-1}), was used to reduce the samples (50 mg) by heating from room temperature to 1050°C at the rate of $10^\circ\text{C}/\text{min}$. Before starting the TPR analyses, the catalysts were pretreated flowing He (50 ml min^{-1}) at 750°C for 60 min and then cooling down.

Scanning electron microscopy (SEM) was performed using a FEI Quanta 200 ESEM microscope, operating at 20 kV on specimens upon which a thin layer of gold had been evaporated. UV–vis spectra were recorded in the diffuse reflectance mode (DRS) in air at room temperature in the wavelength range $190\text{--}800\text{ nm}$ using a Shimadzu UV-2401 PC spectrophotometer, with BaSO_4 as the reference material. Infrared spectra of the samples in KBr (Aldrich) pellets were obtained with a FTIR-8400 Shimadzu spectrometer and the spectra were recorded with 4 cm^{-1} resolution and 256 scans.

The X-ray photoelectron spectroscopy analyses were performed with a VG Microtech ESCA 3000 Multilab, equipped with a dual Mg/Al anode. The spectra were excited by the unmonochromatized Al $K\alpha$ source (1486.6 eV) run at 14 kV and 15 mA. The analyser operated in the constant analyser energy (CAE) mode. For the individual peak energy regions, a pass energy of 20 eV set across the hemispheres was used. Survey spectra were measured at 50 eV pass energy. The sample were analyzed as powders mounted on a double-sided adhesive tape. The constant charging of the samples was removed by referencing all the energies to the C 1s set at 285.1 eV, arising from the adventitious carbon. The invariance of the peak shapes and widths at the beginning and at the end of the analyses ensured the absence of differential charging. Analyses of the peaks were performed with the software provided by VG, based on non-linear least squares fitting programme using a weighted sum of Lorentzian and Gaussian component curves after background subtraction according to Shirley and Sherwood [32,33]. Atomic metal percentage content was calculated from peak intensity using the sensitivity factors provided with the software. The binding energy values were quoted with a precision of $\pm 0.15\text{ eV}$ and the atomic percentage with a precision of $\pm 10\%$.

Thermogravimetric analyses (TGA) were performed with a TGA/DSC1 STAR system Mettler Toledo. Before carrying out the TGA experiments a pretreatment of the samples (10 mg) was performed in N_2 (30 ml min^{-1}) at 750°C for 1 h (step 1) and then the material

Table 1
Crystallite size, specific surface area (SSA) and band gap energy of the prepared catalyst.

Sample	Label	XRD crystallite size (nm)	SSA ($\text{m}^2\text{ g}^{-1}$)	E_{gap} (eV)
$\text{La}_{0.6}\text{Sr}_{0.4}\text{Co}_{0.2}\text{Fe}_{0.8}\text{O}_{3-\delta}$	LSCF6428	31.0	9.5	3.2
$\text{La}_{0.6}\text{Sr}_{0.4}\text{Co}_{0.8}\text{Fe}_{0.2}\text{O}_{3-\delta}$	LSCF6482	29.0	11.0	1.9
$\text{La}_{0.6}\text{Sr}_{0.4}\text{CoO}_{3-\delta}$	LSC64	21.0	16.0	1.9
LaCoO_3	LC	42.0	8.0	2.1
$\text{La}_{0.5}\text{Sr}_{0.5}\text{Co}_{0.8}\text{Fe}_{0.2}\text{O}_{3-\delta}$	LSCF5582	28.0	15.0	2.1
$\text{La}_{0.5}\text{Sr}_{0.5}\text{CoO}_{3-\delta}$	LSC55	39.0	8.7	2.0
$\text{La}_{0.8}\text{Sr}_{0.2}\text{CoO}_{3-\delta}$	LSC82	42.0	7.0	2.0

was cooled down to room temperature in air (30 ml min^{-1}) (step 2). Hence the samples were purged with N_2 (30 ml min^{-1}) for 30 min (step 3) and the TGA experiments were carried out always under N_2 (30 ml min^{-1}) but by heating (5°C/min) from room temperature up to 1100°C (step 4). The evolution of chemisorbed oxygen species, released by the sample, was monitored by on line mass quadrupole (ThermostarTM, Balzers).

2.3. Photoreactivity experiments

Photoreactivity runs were carried out in a gas–solid regime photoreactor, irradiated by natural outdoor solar light. The cylindrical shaped batch type Pyrex fixed bed photoreactor ($V = 100 \text{ ml}$, $\Phi = 94 \text{ mm}$, height = 15 mm) contained 0.1 g of photocatalyst dispersed as a thin layer on the bottom of the photoreactor and the corresponding fixed bed height was ca. 1 mm . After purging pure O_2 for 30 min, $10 \mu\text{L}$ of liquid 2-propanol were injected and quickly vaporized with an infrared gun. The initial nominal concentration of 2-propanol in the gas phase was $1.3 \times 10^{-3} \text{ M}$. The reactor was horizontally positioned and illuminated from the top by the natural solar direct radiation. The solar irradiance reaching the photoreactor was measured each minute by using a Delta Ohm DO 9721 radiometer accessorized with two heads, one measuring UV radiation ($315\text{--}400 \text{ nm}$) and the other the visible one ($400\text{--}950 \text{ nm}$). The runs lasted ca. 5.5 h and the reacting fluid was analyzed by withdrawing gas samples from the photoreactor by means of a gas-tight syringe. Substrate and intermediates concentrations were measured by a GC-17A Shimadzu gas chromatograph equipped with a HP-1 column and a FID, whereas carbon dioxide was analyzed by a Carboxen column in a HP6890 gas chromatograph equipped with a TCD.

Irradiation started only when steady state conditions had been achieved, i.e. after that the system was maintained under dark conditions at room temperature to achieve the adsorption equilibrium of the substrate onto the catalyst surface.

3. Results and discussion

3.1. Characterization of the perovskites

The XRD patterns of Sr substituted LaCoO_3 (LSC) and both Sr and Fe substituted LaCoO_3 (LSCF) perovskites are shown in Fig. 1 (A) and (B), respectively.

The results indicate that the citrate sol–gel method allowed to obtain the desired crystalline structure since 800°C with small crystal size ($20\text{--}40 \text{ nm}$) and surface areas between 7 and $16 \text{ m}^2 \text{ g}^{-1}$. Generally, pure perovskite phases were formed. LC and LSC perovskites showed typical monoclinic structure with space group $I12/a1$, while LSCF perovskites were rhombohedral with R-3CH space group [34,35]. In the XRD patterns of the samples LSC55 and LSCF5582 peaks of secondary phases, LaSrCoO_4 and Co_3O_4 (estimated less than $5 \text{ wt}\%$) were observed, besides the perovskite structure. The presence of such impurities, detected only for the highest Sr content, can be ascribed to the different ionic radius La^{3+} 1.032 \AA , Sr^{2+} 1.18 \AA [36] that affects the crystal strain and symmetry. A pure perovskite phase was formed at higher temperature, after calcining the samples LSC55 and LSCF5582 at 1000°C , but with a dramatic decrease of surface area ($<5 \text{ m}^2 \text{ g}^{-1}$). Consequently the catalysts herein discussed have been calcined at 800°C . Table 1 summarizes the crystallite size, specific surface area and band gap of the perovskite materials along with the chemical composition and labelled name.

Temperature-programmed reduction (TPR) experiments were carried out in order to study the oxygen mobility and the amount of oxygen which can be released from the oxides through the reaction

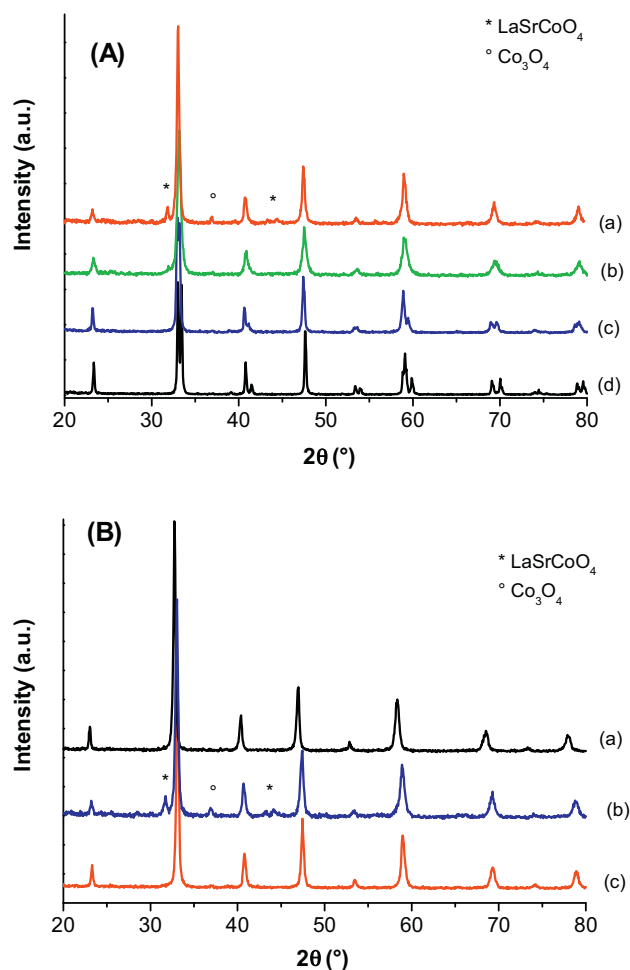


Fig. 1. (A) XRD patterns of LSC perovskites: (a) LSC55; (b) LSC64; (c) LSC82; (d) LC. (B) XRD patterns of LSCF perovskites: (a) LSCF6428; (b) LSCF5582; (c) LSCF6482.

with H_2 . Fig. 2(A) shows the TPR curves of the undoped LC and LSC perovskites. According to the literature the Co^{3+} present in the LC was reduced in two steps: $\text{Co}^{3+} \rightarrow \text{Co}^{2+}$ and $\text{Co}^{2+} \rightarrow \text{Co}^0$ [37,38]. The first process corresponds to a one-electron reaction and occurred in the temperature range $300\text{--}400^\circ\text{C}$ with a maximum at 368°C (see Fig. 2(A) (d)), whereas the second reduction step is a two-electron process that took place between 450 and 650°C with a TPR broad peak centred at 555°C . Table 2 reports the H_2 amount consumed in these reactions, evidencing that the experimental values for LC coincide with the theoretical ones. Also in the LSC perovskites the reduction process of $\text{Co}^{3+} \rightarrow \text{Co}^0$ occurred in two steps, as above mentioned, however, the presence of Sr^{2+} promoted the reduction of some Co^{3+} species to Co^{2+} at lower temperatures. In fact, as shown in Fig. 2(A), the corresponding peak is shifted with a maximum at ca. 290°C , particularly for LSC55 and LSC64. The remaining Co^{3+} and Co^{2+} species were completely reduced to Co^0 in the range $350\text{--}650^\circ\text{C}$. Indeed, as reported in Table 2, the experimental H_2 consumption was higher than the expected one for the $\text{Co}^{2+} \rightarrow \text{Co}^0$ reduction, suggesting the contemporaneous occurrence of the reaction $\text{Co}^{3+} \rightarrow \text{Co}^{2+}$.

The consumption of H_2 due to the first reduction step of Co ($\text{Co}^{3+} \rightarrow \text{Co}^{2+}$) decreased by increasing the amount of Sr in the LSC perovskites. Indeed, 45.2 ml/g of H_2 were consumed by LC for the first reduction step of cobalt but this value progressively decreased from LSC82 to LSC64 up to LSC55 that consumed only 27.6 ml/g . This finding can be explained by considering that the Sr^{2+} introduction enhanced the oxygen vacancies content and consequently

Table 2H₂ (ml/g) consumption and temperatures of reduction peaks for LC, LSC82, LSC64, LSC55 perovskites.

	Reduction steps	Partial experimental consumption (ml/g)	Total experimental consumption (ml/g)	Theoretical consumption (ml/g)	Total reductions (%)
LC	Co ³⁺ → Co ²⁺	45.2 (368 °C)	45.2	45.6 (Co ³⁺ → Co ²⁺)	99.1 (Co ³⁺ → Co ²⁺)
	Co ²⁺ → Co ⁰	90.7 (555 °C)	90.7	91.2 (Co ²⁺ → Co ⁰)	99.5 (Co ²⁺ → Co ⁰)
	Total consumption		135.9	136.8	99.3
LSC82	Co ³⁺ → Co ²⁺	41.4 (344 °C)	41.4	47.6 (Co ³⁺ → Co ²⁺)	87.0 (Co ³⁺ → Co ²⁺)
	Co ²⁺ → Co ⁰	51.3 (445 °C)	91.4	95.1 (Co ²⁺ → Co ⁰)	96.1 (Co ²⁺ → Co ⁰)
	Total consumption	40.1 (540 °C)	132.8	142.7	93.1
LSC64	Co ³⁺ → Co ²⁺	38.5 (283 °C)	38.5	49.7 (Co ³⁺ → Co ²⁺)	77.5 (Co ³⁺ → Co ²⁺)
	Co ³⁺ → Co ²⁺	63.0 (378 °C)	109.0	99.5 (Co ²⁺ → Co ⁰)	(Co ²⁺ → Co ⁰)
	Co ²⁺ → Co ⁰	20.3 (445 °C)			
		25.7 (627 °C)			
LSC55	Co ³⁺ → Co ²⁺	27.6 (295 °C)	27.6	50.9 (Co ³⁺ → Co ²⁺)	54.2 (Co ³⁺ → Co ²⁺)
	Co ³⁺ → Co ²⁺	19.4 (341 °C)	123.2	101.8 (Co ²⁺ → Co ⁰)	(Co ²⁺ → Co ⁰)
	Co ²⁺ → Co ⁰	46.4 (405 °C)			
Total consumption		35.8 (477 °C)			
		21.6 (661 °C)			
			150.8	152.7	98.8

the Co²⁺/Co³⁺ ratio increased (see also XPS and TGA data in the following).

Fig. 2(B) shows the TPR curves of the LSCF perovskites. H₂-TPR profiles of LSCF samples show a first reduction step in the range 300–400 °C attributed to the contemporaneous reductions

of both Co³⁺ → Co²⁺ and Fe³⁺ → Fe²⁺ (see Table 3 for H₂ consumption). Moreover, the LSCF6482 shows a second reduction step with a sharp peak centred at 570 °C corresponding to the reduction Co²⁺ → Co⁰. Eventually, the reduction of Fe²⁺ → Fe⁰ took place at ca. 800–1000 °C. It is worth to note, for the LSCF5582, a shift of the Co²⁺ → Co⁰ reduction step from 570 °C to 415 °C. This insight can be explained by assuming that the highest Sr content promotes the reduction process. LSCF6428 perovskite exhibited the highest H₂ consumption (82.9 ml/g, see Table 3) from 600 °C to over 1000 °C, equivalent to consecutively reductions of both Co²⁺ → Co⁰ and Fe²⁺ → Fe⁰.

The morphology of the samples, studied by SEM analysis, indicate that all the perovskite powders were agglomerates of particles whose sizes depended on the chemical composition of the solid. Some selected SEM microphotographs for the LaCoO₃ based materials are reported in Fig. 3. The morphology of LSCF6482 and LSCF5582 samples, that slightly differ in the La/Sr ratio, were very similar and the particles size were ca. 80 nm. On the contrary, by changing the amount of Fe, that partially substitute Co, the particles size increased from ca. 80 nm to ca. 100–200 nm in LSCF6482 and LSCF6428 samples, respectively. Remarkably, when Sr partially substituted La, in the absence of Fe, in the LSC64 sample, the particles size decreased to 40 nm. Moreover in this sample the constituting particles agglomerated to form flakes whose thickness was ca. 40–60 nm. It is worth to note that also the other two samples in which Sr partially substitutes La, but where Fe is absent, i.e. LSC55 and LSC82, not shown in Fig. 3 for the sake of brevity, showed this particular manner to agglomerate, however in this case the thickness of the flakes was greater (ca. 80–100 nm). Summarizing, it seems that the presence of Sr gave rise to a decrease on the particle size and conversely, the presence of Fe to an increase. It is worth to note that the particles size of the undoped LaCoO₃ sample were in the range 80–160 nm. As far as the amounts of La, Co, Fe and Sr present in the prepared samples are concern, their average values measured by EDX analyses resulted almost equal to the nominal ones, as reported in Table 4.

Regarding to UV–vis absorption properties, the diffuse reflectance spectra of the materials evidenced a strong absorption of light in the visible range. Reflectance (R_{∞}) was transformed to a magnitude proportional to the extinction coefficient (K) through the Kubelka–Munk function, $F(R_{\infty})$ and that was used for the estimation of the optical band gap energies of the perovskites. The band gap value was obtained, as shown in Fig. 4, by extrapolating a linear fitting in the plot of $(F(R_{\infty}) \times E)^2$ vs. the incident light energy, in eV,

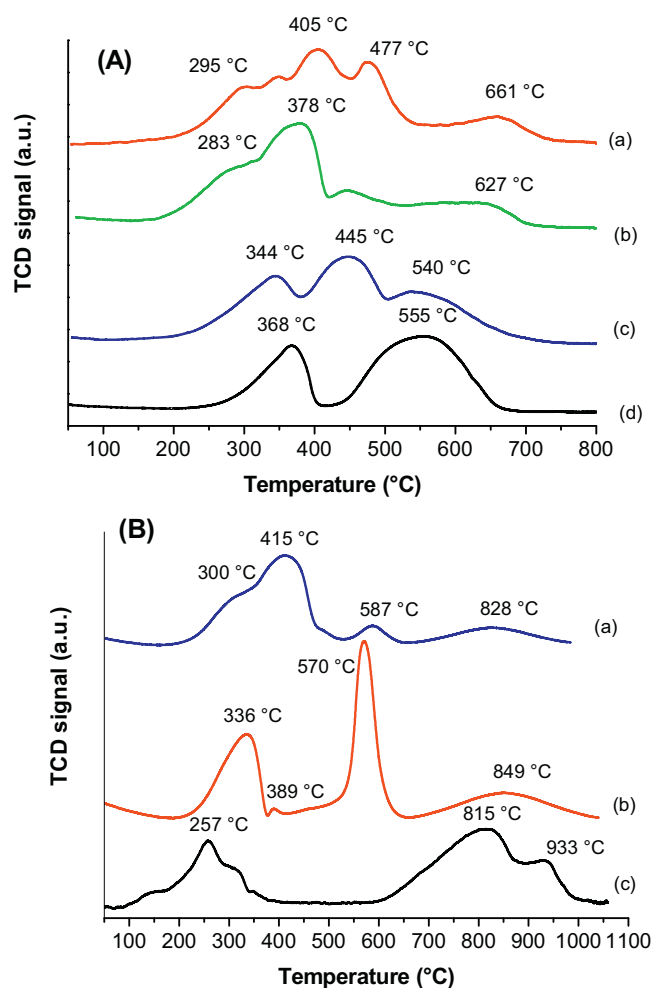
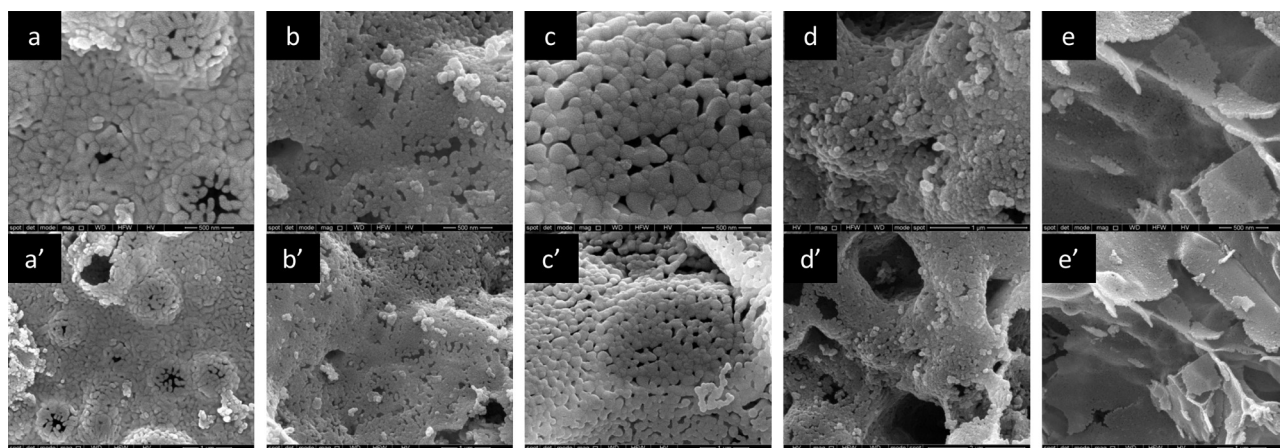


Fig. 2. (A) H₂-TPR curves of LSC perovskites: (a) LSC55; (b) LSC64; (c) LSC82; (d) LC. (B) H₂-TPR curves of LSCF perovskites: (a) LSCF5582; (b) LSCF6482; (c) LSCF6428.

Table 3H₂ (ml/g) consumption and temperatures of reduction peaks for LSCF6482, LSCF5582, LSCF6428 perovskites.

	Reduction steps	Partial experimental consumption (ml/g)	Total experimental consumption (ml/g)	Theoretical consumption (ml/g)	Total reductions (%)
LSCF6482	Co ³⁺ → Co ²⁺	36.8 (336 °C)	38.8	39.9 (Co ^{3+/2+})	77.7 (Co ^{3+/2+} + Fe ^{3+/2+})
	+ Fe ³⁺ → Fe ²⁺	2.0 (389 °C)		10.0 (Fe ^{3+/2+})	
	Co ²⁺ → Co ⁰	58.4 (570 °C)	83.8	(49.9 TOT)	84.0 (Co ^{2+/0} + Fe ^{2+/0})
	+ Fe ²⁺ → Fe ⁰	25.4 (849 °C)		79.8 (Co ^{2+/0})	
Total consumption			122.6	149.6	81.9
LSCF5582	Co ³⁺ → Co ²⁺	28.5 (300 °C)	28.5	40.8 (Co ^{3+/2+})	55.9 (Co ^{3+/2+} + Fe ^{3+/2+})
	+ Fe ³⁺ → Fe ²⁺			10.2 (Fe ^{3+/2+})	
	Co ²⁺ → Co ⁰	42.5 (415 °C)	64.5	(51.0 TOT)	63.2 (Co ^{2+/0} + Fe ^{2+/0})
	+ Fe ²⁺ → Fe ⁰	6.8 (587 °C)		81.7 (Co ^{2+/0})	
Total consumption			93.0	153.1	60.7
LSCF6428	Co ³⁺ → Co ²⁺	33.1 (257 °C)	33.1	10.1 (Co ^{3+/2+})	65.8 (Co ^{3+/2+} + Fe ^{3+/2+})
	+ Fe ³⁺ → Fe ²⁺			40.2 (Fe ^{3+/2+})	
	Co ²⁺ → Co ⁰	61.3 (815 °C)	82.9	(50.3 TOT)	82.4 (Co ^{2+/0} + Fe ^{2+/0})
	+ Fe ²⁺ → Fe ⁰	21.6 (933 °C)		20.1 (Co ^{2+/0})	
Total consumption			116.0	150.9	76.8

**Fig. 3.** SEM micrographs for (a), (a') LSCF6428; (b), (b') LSCF6482; (c), (c') LC; (d), (d') LSCF5582 and (e), (e') LSC64 samples with two different enlargements.

as suggested by Tauc [39], by considering all the perovskite samples as direct band gap semiconductors. The obtained values are reported in Table 1. LC sample showed a band gap energy of 2.1 eV, in agreement with the literature reported data [22]. Korotin et al. [40], theoretically calculated the band gap in LaCoO₃ considering a rhombohedral distorted phase and estimated a direct band gap of ca. 2.07 eV. When Sr²⁺ partially substitute La, in the absence of Fe²⁺, no appreciable change in the band gap was observed. Slight differences on the estimated band gap values between the LSC samples can be related to slight differences in the crystallites size but

also to differences in the electronic band structures due to the created oxygen vacancies. The presence of Fe²⁺ clearly modifies the UV absorption properties of the LC perovskite. The sample LSCF6428 that contained the higher amount of Fe showed the highest value of band gap (3.2 eV). This wide band gap can be related to the less significant oxygen lattice defects as observed by XPS analyses (see below).

These results allow to conclude that the presence of Sr²⁺ does not change significantly the band gap of the perovskite whereas the presence of Fe²⁺ increase it.

Table 4

Nominal and measured by EDX and XPS compositions of the used samples.

Sample	EDX atomic %				XPS atomic %				Nominal atomic %			
	La	Sr	Co	Fe	La	Sr	Co	Fe	La	Sr	Co	Fe
LSCF6428	29	22	9	40	26	37	14	23	30	20	10	40
LSCF6482	26	22	42	10	22	30	42	5	30	20	40	10
LSC64	27	23	50	0	26	37	37	0	30	20	50	0
LC	46	0	54	0	65	0	35	0	50	0	50	0
LSCF5582	22	23	44	10	24	42	26	8	25	25	40	10
LSC55	25	25	50	0	–	–	–	–	25	25	50	0
LSC82	35	12	53	0	–	–	–	–	40	10	50	0

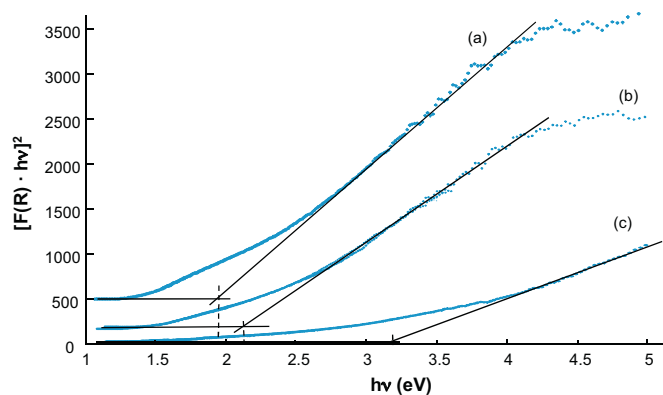


Fig. 4. Tauc plot of selected perovskite samples: (a) LSCF6482; (b) LC; (c) LSCF 6428.

Some of the XPS results are summarized in Table 5, which lists the binding energy relative to the elements, more influenced by the composition of the LSCF samples.

The O 1s region is shown in Fig. 5 for three selected samples, LSC64, LSCF6482 and LSCF6428. Three components at ca. 529, 531 and 532 eV attributed to lattice, surface and adsorbed oxygen, respectively are clearly visible (see Fig. 5 inset) [41–43]. The adsorbed oxygen has been omitted in Table 5 and only the lattice and surface components has been used to calculate the relative amount of the two types of oxygen. The more interesting feature, looking at the oxygen component, is that the lattice component increased by increasing the iron content, pointing out to a decrease of the oxygen vacancies in the structure. The Sr 3d region shows for all samples, two doublet with the 3d5/2 component centred at ca. 132 and 134 eV, with the former increasing with the increase of iron content. In Fig. 6 the Sr 3d region is displayed for LSC64, LSCF6482 and LSCF6428. The correct attribution of this pattern for the Sr region is not clear. According to Liu et al. [44] the higher binding energy component is attributed to Sr in the perovskites lattice while the low energy component to Sr²⁺ ion surrounded by oxygen vacancies in the perovskites. Another hypothesis [43,45] attributed the lower binding energy to the bulk component while the higher component to surface segregated strontium. By considering the trends of both oxygen and strontium it can be observed that, actually, the higher Sr binding energy component increases when the oxygen lattice decreases, i.e. with the increase of the oxygen vacancies. Cobalt region shows the typical Co 2p pattern

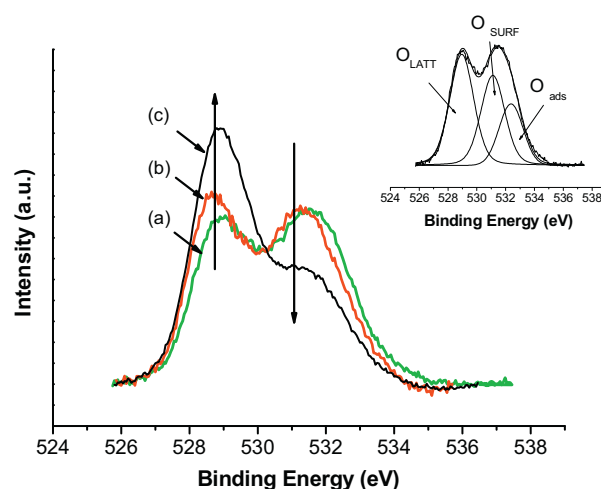


Fig. 5. O 1s region of (a) LSC64, (b) LSCF6482, (c) LSCF6428. The arrows indicate the direction of the two components with the increasing of iron content. In the inset the fitting showing the three components is displayed for LSC64 sample.

with the two Co 2p_{3/2} and Co 2p_{1/2} spin-orbit components separated by 15.5 eV and by two satellite peaks (shake up). By the curve fitting routine, two Co 2p_{3/2} binding energy at ca. 780 and 782 were obtained and according to Prasad [43] they are attributed to Co³⁺ and Co²⁺, respectively. The undoped LC sample shows the presence of Co³⁺ while all doped samples presented both Co²⁺ and Co³⁺ and according with the TPR results the relative amount of Co²⁺ increased with the increasing of the Fe²⁺ content. The surface composition, measured by XPS, is listed in Table 4 along with the EDX bulk results and the nominal atomic metal percentage. Contrary to the EDX results, which refers to bulk composition, a segregation of the A site cations, especially of Sr, on the surface is observed for all the samples. This phenomenon has been already observed for similar systems and does not seem to be influenced by the differences in the composition [46,47].

TGA experiments were carried out in order to study the oxygen vacancies content in the perovskites induced by Sr doping and/or by the Co/Fe content. In Fig. 7 the weight loss percentages vs. temperature are displayed for selected samples, while in Table 6 the weight loss values are reported. It is worth noting that the weight loss, due to oxygen species desorption, increased from LC to LSCF perovskites according to the defects generated by Sr doping.

Table 5
XPS binding energies relative to some elements present in the perovskite samples.

	O 1s	Sr3d5/2	Co 2p1/2
LSCF6428	528.8 (75%) 530.7 (25%)	132.4 (76%) 134.4 (24%)	779.7 Co(III) (39%) Co(II) (61%)
LSCF6482	528.7 (55%) 530.9 (45%)	132.3 (63%) 134.8 (37%)	779.9 Co(III) (42%) Co(II) (58%)
LSC64	529.0 (55%) 531.1 (45%)	132.6 (49%) 134.5 (51%)	780.3 Co(III) (53%) Co(II) (47%)
LC	528.9 (63%) 531.0 (37%)	–	779.8 Co(III) (100%)
LSCF5582	528.9 (60%) 531.1 (40%)	132.2 (55%) 134.3 (45%)	779.8 Co(III) (48%) Co(II) (52%)

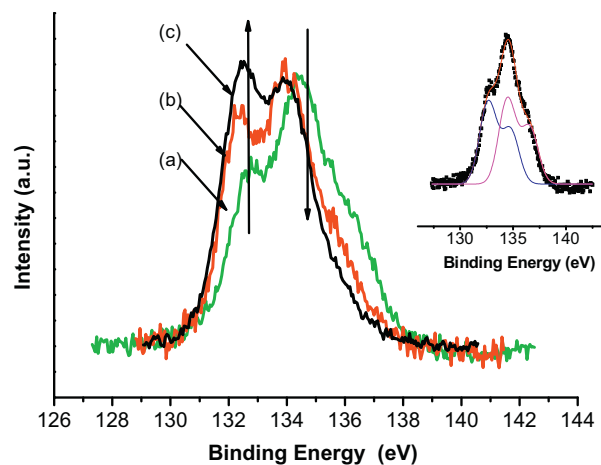


Fig. 6. Sr 3d region of (a) LSC64, (b) LSCF6482, (c) LSCF6428. The arrows indicate the direction of the two components with the increasing of iron content. In the inset the fitting showing the three component is displayed for LSC64 sample.

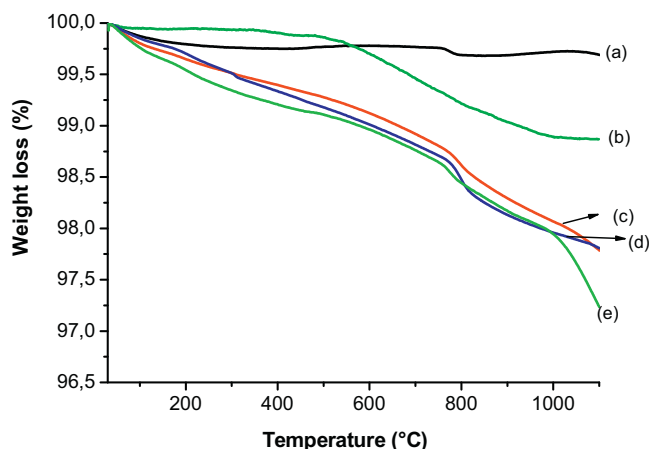


Fig. 7. TGA curves registered for LC, LSC and LSCF perovskites: (a) LC; (b) LSCF6428; (c) LSCF6482; (d) LSCF5582; (e) LSC64.

Indeed, the highest the defects content in the perovskite lattice, the highest the oxygen chemisorption capacity and release. In our experiment, the oxygen will fill the perovskite vacancies when material was cooled down to room temperature in air (see TGA experimental part (step 2)). Then during the step 4, the oxygen previously chemisorbed is again released.

By comparing LSC64 with LSC6482 and LSC6428, it can be noted that the weight loss percentage decreased by increasing Fe content, in well agreement with XPS data, suggesting a decrease of oxygen vacancies with the increase of the iron content. The sample LSC64 without any iron exhibited the highest oxygen chemisorption capacity showing in the TGA experiment the highest weight loss due to O_2 evolution.

3.2. Photoreactivity experiments

Blank reactivity experiments were performed under the same experimental conditions used for the photo-reactivity runs but in the absence of catalyst, oxygen or light. No reactivity was observed in all these cases so that it was concluded that the contemporary presence of O_2 , catalyst, and irradiation was needed for the occurrence of the 2-propanol degradation process.

The photoreactivity runs started after the system achieved the steady state conditions in the dark, i.e. when the concentration of 2-propanol remained constant with time (ca. 0.5 h). 2-propanol was partially adsorbed on the perovskite samples; indeed, after the equilibration time, the initial substrate concentration, experimentally measured, was always lower than the nominal amount. During the 2-propanol degradation, traces of acetaldehyde and propanone as the main intermediates were observed along with traces of CO_2 as final oxidation product. In order to compare the photoreactivity results obtained under natural sunlight irradiation, the cumulative photon energy, E , incident on the reactor was calculated from the experimental measurement of the irradiance.

Table 6
TGA weight loss percentage for some selected samples.

Sample	Weight loss %
LC	0.31
LSCF6428	1.13
LSCF5582	2.20
LSCF6482	2.22
LSC64	2.78

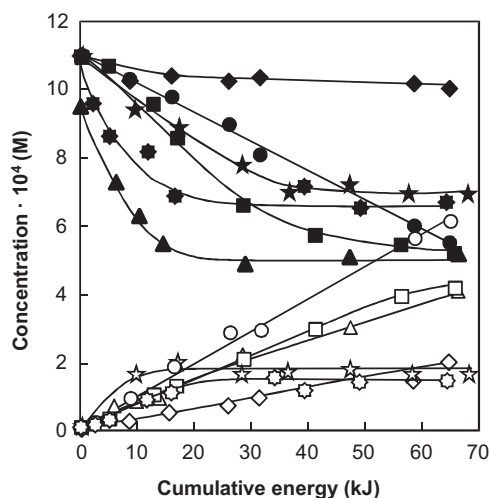


Fig. 8. Evolution of 2-propanol (full symbol) and propanone (empty symbol) concentrations vs. cumulative energy for runs carried out in the presence of (♦, ◇) LSCF6428; (●, ○) LSCF6482; (★, ☆) LSCF5582; (■, □) LC; (●, ✱) LSC55; (▲, △) LSC64.

This quantity is given by:

$$E = \int_0^t I(t) dt \quad (1)$$

in which " $I(t)$ " is the instantaneous photon flow and " t " the irradiation time. The values of " $I(t)$ " were calculated from the recorded values of irradiance, $UVG(t)$, by using the following relationship:

$$I(t) = UVG(t) \cdot S \quad (2)$$

in which " S " is the total irradiated surface and " UVG " is the irradiance (in the 315–730 nm wavelength range).

Fig. 8 reports the concentration evolution of 2-propanol and propanone vs. the cumulative photon energy for runs carried out in the presence of some selected perovskite sample.

Fig. 8 shows that the bare perovskite LC and LSC64 were the most active photocatalysts for the 2-propanol degradation. In the presence of LSC64, which showed the highest 2-propanol adsorption in dark conditions, the 2-propanol concentration reached a plateau after ca. 20 kJ of cumulative photon energy entering the reacting medium. Interestingly, in the same run, the propanone concentration always increased, indicating that after 20 kJ the 2-propanol degradation rate becomes equal to that of 2-propanol adsorption onto the sample surface. LSCF6482 and LSCF5582 samples were slightly less active than LC and LSC64. On the contrary, the reactivity of LSCF6428 was very poor.

Some considerations on the photoreactivity of the prepared perovskites can be done by taking into account the influence of the presence of Sr and/or Fe partially substituting La or Co, respectively in the $LaCoO_3$ sample.

In particular, the material with the smaller amount of Sr (LSC82) showed negligible photoactivity. On the contrary, by increasing the amount of Sr, as in the LSC64, the reactivity was slightly higher on respect to that of LC, however, the adsorption of 2-propanol was higher and this can be related to the increased surface area (from 8.0 to 16.0 $m^2 g^{-1}$). Finally, the sample with the highest amount of Sr (LSC55) presented the same initial photoactivity of LC but it deactivated after ca. 20 kJ of cumulative photon energy.

It is worth to note that there is an evident difference between LC and LSC64 in terms of oxygen vacancies because the presence of Sr^{2+} seems to increase the oxygen lattice defects, as shown by XPS analyses. The oxygen vacancies in a perovskite crystalline structure increased the oxygen adsorption ability [48], in agreement with the current TGA experiment observations. This phenomenon,

preventing the electron-hole recombination, could improve also the photocatalytic activity of the material [49]. It is worth to remind that the presence of oxygen defects favours the electronic delocalization and hence a narrowing of the forbidden band gap occurred [49]. Consequently, the slightly lower band gap energy showed by the LSC64 sample with respect to LC can also be attributed to the oxygen defects that help to increase its photocatalytic activity.

When Fe was added to LSC55 obtaining LSCF5582 sample the photoactivity decreased. On the contrary, an interesting effect of the partial substitution of Co with Fe in the LSC64 catalyst to obtain LSCF6482 and LSCF6428 sample was observed. In particular, the LSCF6482 sample showed lower photoactivity than the LSC64 material. This effect can be related to the decrease in the specific surface area (from 16 to 11 m² g⁻¹). A perusal of Fig. 8 indicates that by using LSCF6482 the concentration of 2-propanol always decreased as the concentration of propanone always increased indicating that no deactivation of the catalyst occurred, at least up to 65 kJ of cumulative energy entering the photoreactor.

By increasing the amount of Fe (LSCF6428 sample) it was observed a further decrease in the reactivity but also in this case no deactivation of the catalyst occurred. The decrease of the photoactivity, in this last case, is clearly related to the highest band gap of the LSCF6428 sample (3.2 eV) which allows only a small fraction of the cumulative photon energy impinging the reacting medium to be exploited.

These results suggest that the perovskites containing Fe are less active and the activity decreases by increasing the Fe content but also that the presence of iron avoids the catalyst deactivation.

4. Conclusions

LaCoO₃ perovskites substituted by Sr at the A site and/or by Fe at the B site (La_{1-x}Sr_xCo_{1-y}Fe_yO_{3-δ}), showing pure rhombohedral crystallographic phase, have been prepared by the citrate method. TPR analyses evidenced for undoped LaCoO₃ the presence of Co³⁺ species only, while all samples doped at the A and/or at the B sites presented both Co²⁺ and Co³⁺ and the relative amount of Co²⁺ increased by increasing the Fe²⁺ content. This finding suggests the presence of oxygen vacancies in the former samples. XPS data confirmed this trend, highlighting that the introduction of Fe at the B site of the perovskite changed the ratio between the lattice oxygen and the surface one. Interestingly, the lattice component increased by increasing the iron content, pointing out to a decrease of the oxygen vacancies in the structure. These materials showed photocatalytic activity for the 2-propanol degradation in the gas–solid regime irradiating by natural solar light. The photoreactivity of the prepared perovskites was influenced by the presence of Sr and/or Fe partially substituting La or Co. In particular, the material with the smaller amount of Sr, La_{0.8}Sr_{0.2}CoO_{3-δ}, showed negligible photoactivity. On the contrary, by increasing the amount of Sr, as in the La_{0.6}Sr_{0.4}CoO_{3-δ}, the reactivity was slightly higher on respect to that of LaCoO₃. Moreover, the perovskites containing Fe are less active and the activity decreases by increasing the Fe content, however, the presence of iron avoids the catalyst deactivation.

The sample La_{0.6}Sr_{0.4}CoO_{3-δ} showed the best catalytic activity, likely due to the combination of several factors, such as the optimal crystalline particle sizes and grains dimension, high specific surface area, presence of oxygen vacancies and low band gap energy value.

Acknowledgements

The authors wish to thank MIUR and INCA for financial support. Support by COST Action CM1104 is also kindly acknowledged.

References

- [1] M.R. Hoffmann, S.T. Martin, W. Choi, D.W. Bahnemann, *Chem. Rev.* 95 (1995) 69–96.
- [2] A. Di Paola, L. Palmisano, E. García-López, G. Marci, *J. Hazard. Mater.* 211–212 (2012) 3–29.
- [3] A. Kubacka, M. Fernández-García, G. Colón, *Chem. Rev.* 112 (2012) 1555–1614.
- [4] D.M. Schultz, T.P. Yoon, *Science* 343 (2014) 1239176.
- [5] N. Wang, D. Kong, H. He, *Powder Technol.* 207 (2011) 470–473.
- [6] B. Zhou, X. Zhao, H. Liu, J. Qu, C.P. Huang, *Appl. Catal. B* 99 (2010) 214–221.
- [7] Y. Wan, S. Wang, W. Luo, L. Zhao, *Int. J. Photoenergy* 2012 (2012) 392865–392871.
- [8] L.S. Jia, J.J. Li, W.P. Fang, H. Song, Q.B. Li, Y. Tang, *Catal. Commun.* 10 (2009) 1230–1234.
- [9] S. Zeng, R. Tang, S. Duan, L. Li, C. Liu, X. Gu, S. Wang, D. Sun, *J. Colloid Interface Sci.* 432 (2014) 236–245.
- [10] Z.G. Zou, H. Arakawa, *J. Photochem. Photobiol. A* 158 (2003) 145–162.
- [11] A. Nechache, M. Cassir, A. Ringuede, J. Power Sources 258 (2014) 164–181.
- [12] G.F. Fine, L.M. Cavanagh, A. Afonja, R. Binions, *Sensors* 10 (2010) 5469–5502.
- [13] A. Feldhoff, J. Martynczuk, H. Wang, *Prog. Solid State Chem.* 35 (2007) 339–353.
- [14] B. Zhan, J.L. Lan, Y.C. Liu, Y.H. Lin, C.W. Nan, *J. Inorg. Mater.* 29 (2014) 237–244.
- [15] I.E. Wachs, K. Routray, *ACS Catal.* 2 (2012) 1235–1246.
- [16] R.A. Eichel, *Phys. Chem. Chem. Phys.* 13 (2011) 368–384.
- [17] J. Suntivich, H.A. Gasteiger, N. Yabuuchi, H. Nakanishi, J.B. Goodenough, Y. Shao-Horn, *Nat. Chem.* 3 (2011) 546–550.
- [18] J.B. Goodenough, *Rep. Prog. Phys.* 67 (2004) 1915–1993.
- [19] Y. Zhang, J. Hu, E. Cao, L. Sun, H. Quin, *J. Magn. Mater.* 324 (2012) 1770–1775.
- [20] E. Tsipis, V.V. Kharton, *J. Solid State Electrochem.* 12 (2008) 1367–1391.
- [21] S. Wang, M. Katsuki, M. Dokiya, T. Hashimoto, *Solid State Ion.* 159 (2003) 71–78.
- [22] S. Fu, H. Niu, Z. Tao, J. Song, C. Mao, S. Zhang, C. Chen, D. Wang, *J. Alloys Comp.* 576 (2013) 5–12.
- [23] L. Jiang, Z.X. Wei, *Nanoscience* 12 (2007) 20–24.
- [24] B. Dong, Z. Li, Z. Li, X. Xu, M. Song, W. Zheng, C. Wang, S.S. Al-Deyab, M. El-Newehy, *J. Am. Ceram. Soc.* 93 (2010) 3587–3590.
- [25] C. Zhang, H. He, N. Wang, H. Chen, D. Kong, *Ceram. Int.* 39 (2013) 3685–3689.
- [26] Y. Yamada, K. Yano, D. Hong, S. Fukuzumi, *Phys. Chem. Chem. Phys.* 14 (2012) 5753–5760.
- [27] W. Kaituo, W. Xuehang, W. Wenwei, L. Yongni, L. Sen, *Ceram. Int.* 40 (2014) 5997–6004.
- [28] Q. Xu, D. Huang, W. Chen, J. Lee, H. Wang, R. Yuan, *Scr. Mater.* 50 (2004) 165–170.
- [29] S.J. Gregg, K.S. Sing, *Adsorption, Surface Area and Porosity*, 2nd ed., Academic Press, San Diego, 1982.
- [30] *Inorganic Crystal Structure Database*, ICSD, FIZ Karlsruhe, 2014.
- [31] H.P. Klug, L.E. Alexander, *X-ray Diffraction Procedures for Polycrystalline and Amorphous Materials*, Wiley, New York, 1954.
- [32] D.A. Shirley, *Phys. Rev. B* 5 (1972) 4709–4714.
- [33] P.M.A. Sherwood, in: D. Briggs, M.P. Seah (Eds.), *Practical Surface Analysis*, Wiley, New York, 1990, p. 181.
- [34] O. Haas, R.P.W.J. Struis, J.M. McBreen, *J. Solid State Chem.* 177 (2004) 1000–1010.
- [35] F. Puleo, L.F. Liotta, V. La Parola, D. Banerjee, A. Martorana, A. Longo, *Phys. Chem. Chem. Phys.* (2014), <http://dx.doi.org/10.1039/C4CP03214D>.
- [36] R.D. Shannon, *Acta Crystallogr. A* 32 (1976) 751–767.
- [37] I.S. Yakovleva, L.A. Isupova, V.A. Rogov, *Kinet. Catal.* 50 (2009) 275–283.
- [38] N. Russo, S. Furfori, D. Fino, *Appl. Catal. B* 83 (2008) 85–95.
- [39] J. Tauc, *Mater. Res. Bull.* 5 (1970) 37–46.
- [40] M. Korotin, S.Y. Ezhov, I. Solov'yev, V. Anisimov, D. Khomskii, G. Sawatzky, *Phys. Rev. B* 54 (1996) 5309–5316.
- [41] X. Li, H. Zhang, X. Liu, S. Li, M. Zhao, *Mater. Chem. Phys.* 38 (1994) 355–362.
- [42] X. Li, X. Liu, B. Zu, M. Zhao, *J. Alloys Compd.* 186 (1992) 315–319.
- [43] D.H. Prasad, S.Y. Park, E.O. Oh, H.R. Kim, K.J. Son, J.H. Lee, *Appl. Catal. A* 447–448 (2012) 100–106.
- [44] B. Liu, L. Tang, Y. Zhang, *Int. J. Hydrogen Energy* (2009) 440–445.
- [45] P.A.W. Ven der Heide, *Surf. Interface Anal.* 33 (2002) 414–425.
- [46] J. Durce, T. Ishihara, J. Kilner, *Solid State Ion.* 262 (2014) 893–896.
- [47] H. Ding, A.V. Virkar, M. Liu, F. Liu, *Phys. Chem. Chem. Phys.* 15 (2013) 489–496.
- [48] H. Gerisher, A. Heller, *J. Phys. Chem.* 95 (1991) 5261–5267.
- [49] X. Zhao, Q. Yang, J. Cui, *J. Rare Earths* 26 (2008) 511–514.